DESY–22–107
June 2022

Measurement of the cross-section ratio $\sigma_{\psi(2S)}/\sigma_{J/\psi(1S)}$ in exclusive photoproduction at HERA

ZEUS Collaboration

Abstract

The exclusive photoproduction reactions $\gamma p \to J/\psi(1S)p$ and $\gamma p \to \psi(2S)p$ have been measured at an ep centre-of-mass energy of 318 GeV with the ZEUS detector at HERA using an integrated luminosity of $373\,\text{pb}^{-1}$. The measurement was made in the kinematic range $30 < W < 180\,\text{GeV}$, $Q^2 < 1\,\text{GeV}^2$ and $|t| < 1\,\text{GeV}^2$, where W is the photon–proton centre-of-mass energy, Q^2 is the photon virtuality and t is the squared four-momentum transfer at the proton vertex. The decay channels used were $J/\psi(1S) \to \mu^+\mu^-$, $\psi(2S) \to \mu^+\mu^-$ and $\psi(2S) \to J/\psi(1S)\pi^+\pi^-$ with subsequent decay $J/\psi(1S) \to \mu^+\mu^-$. The ratio of the production cross sections, $R = \sigma_{\psi(2S)}/\sigma_{J/\psi(1S)}$, has been measured as a function of W and $|t|$ and compared to previous data in photoproduction and deep inelastic scattering and with predictions of QCD-inspired models of exclusive vector-meson production, which are in reasonable agreement with the data.

1 Introduction

The exclusive photoproduction of vector mesons leads to a simple final-state system, as illustrated in Fig. 1(a). The clean environment and the large masses of the $J/\psi(1S)$ and $\psi(2S)$ mesons facilitate measurements that provide insight into the dynamics of a hard process. The $J/\psi(1S)$ and the $\psi(2S)$ have the same quark content but different radial distributions of the wave functions, and their mass difference is small. Therefore, this measurement allows QCD-inspired predictions of the wave-function dependence of the respective cross sections to be tested. A suppression of the $\psi(2S)$ cross section relative to the $J/\psi(1S)$ is expected, as the $\psi(2S)$ wave function has a radial node close to the typical transverse separation of the virtual $c\bar{c}$ pair. The process is also sensitive to the gluon density in the proton.

The exclusive (also referred to as "elastic") production of a vector meson in ep collisions, in which the proton remains intact, is shown in Fig. 1(a). The proton-dissociative process, where the proton breaks up into a hadronic state denoted as Y, is shown in Fig. 1(b). The two processes have similar experimental signatures and so when the system Y remains undetected, proton-dissociative events form a significant background. The following kinematic variables are used to characterise these processes. The negative squared four-momentum of the exchanged photon, Q^2, is equal to $-q^2 = -(k-k')^2$, where k and k' are the four-momenta of the incoming and outgoing lepton. As $Q^2 \approx 0\,\mathrm{GeV}^2$ in photoproduction and the transverse momentum of the vector meson is small in the present measured kinematic region, the hard QCD scale is provided by the squared mass of the vector meson, M_V^2. The photon–proton centre-of-mass energy, W, is given by $W^2 = (q+P)^2$, where P is the four-momentum of the incoming proton. The squared four-momentum transfer at the proton vertex, t, is given by $t = (P-P')^2$, where P' is the four-momentum of the outgoing proton (or dissociative state Y).

At the HERA ep collider, the ZEUS collaboration has previously measured the exclusive production of $J/\psi(1S)$ and $\psi(2S)$ mesons in deep inelastic scattering (DIS) [1]. The H1 collaboration has also measured the processes in DIS [2], as well as in photoproduction [3, 4]. In these analyses, the ratio of the $\psi(2S)$ to $J/\psi(1S)$ production cross sections, where some of the systematic uncertainties are expected to cancel, was measured and compared with QCD-inspired models. These previous data exhibit an increase in the ratio with increasing Q^2 that is described by many of the QCD models. No dependence of the ratio with W and $|t|$ was observed, although the $|t|$ dependence has so far been measured only in DIS.

In this paper, a new measurement of the ratio of the photoproduction cross sections of the exclusive reactions $ep \rightarrow e\psi(2S)p$ and $ep \rightarrow eJ/\psi(1S)p$ is presented. The ratio is measured differentially as a function of W and $|t|$. The decay channels used were

$J/\psi(1S) \to \mu^+\mu^-$, $\psi(2S) \to \mu^+\mu^-$, and $\psi(2S) \to J/\psi(1S)\,\pi^+\pi^-$ with the subsequent decay $J/\psi(1S) \to \mu^+\mu^-$.

2 Experimental set-up

The measurement is based on data collected with the ZEUS detector at the HERA collider during the period 2003–2007, corresponding to an integrated luminosity of $373\,\text{pb}^{-1}$. During this period, the HERA accelerator collided an electron[1] beam of energy 27.5 GeV with a proton beam of 920 GeV, yielding an *ep* centre-of-mass energy of 318 GeV.

A detailed description of the ZEUS detector can be found elsewhere [5]. A brief outline of the components that are most relevant for this analysis is given below.

In the kinematic range of the analysis, charged particles were mainly tracked in the central tracking detector (CTD) [6–8] and the microvertex detector (MVD) [9]. These components operated in a magnetic field of 1.43 T provided by a thin superconducting solenoid. The CTD consisted of 72 cylindrical drift-chamber layers, organised in nine superlayers covering the polar-angle[2] region $15^\circ < \theta < 164^\circ$. The MVD silicon tracker consisted of a barrel (BMVD) and a forward (FMVD) section. The BMVD contained three layers and provided polar-angle coverage for tracks from 30° to 150°. The four-layer FMVD extended the polar-angle coverage in the forward region to 7°. After alignment, the single-hit resolution of the MVD was 24 µm. The transverse distance of closest approach (DCA) of a track to the nominal vertex in X–Y was measured to have a resolution, averaged over the azimuthal angle, of $(46 \oplus 122/p_T)$ µm, with p_T in GeV denoting the momentum transverse to the beam axis. For CTD–MVD tracks that pass through all nine CTD superlayers, the momentum resolution was $\sigma(p_T)/p_T = 0.0029 p_T \oplus 0.0081 \oplus 0.0012/p_T$, with p_T in GeV.

The high-resolution uranium–scintillator calorimeter (CAL) [10–13] consisted of three parts: the forward (FCAL), the barrel (BCAL) and the rear (RCAL) calorimeters. Each part was subdivided transversely into towers and longitudinally into one electromagnetic section (EMC) and either one (in RCAL) or two (in BCAL and FCAL) hadronic sections (HAC). The smallest subdivision of the calorimeter was called a cell. Adjacent cells were combined to form clusters. The CAL energy resolutions, as measured under test-beam

---

[1] Hereafter, "electron" refers to both electrons and positrons unless otherwise stated.

[2] The ZEUS coordinate system is a right-handed Cartesian system, with the Z axis pointing in the nominal proton beam direction, referred to as the "forward direction", and the X axis pointing left towards the centre of HERA. The coordinate origin is at the centre of the CTD. The pseudorapidity is defined as $\eta = -\ln\left(\tan\frac{\theta}{2}\right)$, where the polar angle, θ, is measured with respect to the Z axis. The azimuthal angle, φ, is measured with respect to the X axis.

conditions, were $\sigma(E)/E = 0.18/\sqrt{E}$ for electrons and $\sigma(E)/E = 0.35/\sqrt{E}$ for hadrons, with E in GeV.

The muon system consisted of rear, barrel (R/BMUON) and forward (FMUON) tracking detectors. The R/BMUON consisted of limited-streamer (LS) tube chambers placed behind the RCAL (BCAL), inside and outside a magnetised iron yoke surrounding the CAL. The barrel and rear muon chambers covered polar angles from 34° to 135° and from 135° to 171°, respectively. The FMUON consisted of six trigger planes of LS tubes and four planes of drift chambers covering the angular region from 5° to 32°. The muon system exploited the magnetic field of the iron yoke and, in the forward direction, of two iron toroids magnetised to $\approx 1.6\,\text{T}$ to provide an independent measurement of the muon momenta.

The iron yoke surrounding the CAL was instrumented with proportional drift chambers to form the backing calorimeter (BAC) [14]. The BAC consisted of 5142 aluminium chambers inserted into the gaps between 7.3 cm thick iron plates (10, 9 and 7 layers in the forward, barrel and rear directions, respectively). The chambers were typically 5 m long and had a wire spacing of 1.5 cm. The anode wires were covered by 50 cm long cathode pads. The BAC was equipped with energy readout and position-sensitive readout for muon tracking. The former was based on 1692 pad towers ($50 \times 50\,\text{cm}^2$), providing an energy resolution of $\sigma(E)/E \approx 100\%/\sqrt{E}$, with E in GeV. The position information from the wires allowed the reconstruction of muon trajectories in two dimensions (XY in the barrel and YZ in the endcaps) with a spatial accuracy of a few mm.

The luminosity was measured using the Bethe–Heitler reaction $ep \to e\gamma p$ by a luminosity detector which consisted of independent lead–scintillator calorimeter [15–17] and magnetic spectrometer [18, 19] systems.

3 Monte Carlo simulations

Free parameters within the Monte Carlo (MC) simulations, which control the kinematic dependences of the reactions of interest, have been tuned to previous data. The values have been checked here and either used where appropriate or tuned to the data presented in this paper.

The DIFFVM [20] MC program was used for simulating the photoproduction of exclusive heavy vector mesons, $ep \to eVp$, where V denotes the produced vector meson. For the event generation, the following cross-section parameterisations were used:

- $(1 + Q^2/M_V^2)^{-1.5}$ for the dependence on Q^2;

- W^δ, with $\delta = 0.67$ [21] and $\delta = 1.1$ [22] for the dependence on W of the total cross section for $J/\psi(1S)$ and $\psi(2S)$ events, respectively;
- $\exp(-b\,|t|)$, with $b = 4.6\,\text{GeV}^{-2}$ and $b = 4.3\,\text{GeV}^{-2}$ for the dependence on $|t|$ for $J/\psi(1S)$ and $\psi(2S)$ events, respectively [3];
- the b values were re-weighted according to the formula $b' = b + 4\,\alpha' \ln(W/W_0)$, where $W_0 = 90\,\text{GeV}$ and α' is determined to be $0.12\,\text{GeV}^{-2}$ [23];
- s-channel helicity conservation for the production of $V \to \mu^+\mu^-$;
- a reweighting for the pion phase space [24] using the function $(M(\pi^+,\pi^-)^2 - 4\,M_\pi^2)^2$, where $M(\pi^+,\pi^-)$ is the invariant mass of the two pions in the $\psi(2S) \to J/\psi(1S)\pi^+\pi^-$ decay and M_π is the mass of the charged pion.

Proton-dissociative $J/\psi(1S)$ and $\psi(2S)$ events were also simulated with the DIFFVM MC program with parameters:

- $\delta = 0.42$ [21] and $\delta = 0.70$ (tuned here) for the W dependence for $J/\psi(1S)$ and $\psi(2S)$ events, respectively;
- $b = 1.0\,\text{GeV}^{-2}$ and $b = 0.7\,\text{GeV}^{-2}$ for the respective t dependences [3];
- the dependence on the mass of the dissociated proton system, M_Y, was simulated as $1/M_Y^\beta$, with $\beta = 2.4$ (tuned here) for both $J/\psi(1S)$ and $\psi(2S)$ production above the proton-resonance region, i.e. $M_Y \gtrsim 2\,\text{GeV}$.

Non-resonant electroweak dimuon production (Bethe–Heitler process) was simulated using the program GRAPE [25]. The MC sample contains both exclusive and proton-dissociative events.

The generated MC events were passed through the ZEUS detector and trigger simulation programs based on GEANT 3 [26]. They were then reconstructed and analysed with the same programs as used for the data.

4 Event selection and signal extraction

4.1 Event selection

Events that contained signals from the decay products of the $\psi(2S)$ or $J/\psi(1S)$ but no other activity in the central ZEUS detector were selected. Only final states containing muons were considered.

A three-level trigger system [5, 27, 28] was used to select events online. The principal requirement for muon-candidate events was at least one CTD track matched to a cluster consistent with a minimum-ionising particle in the CAL and associated with a F/B/RMUON deposit or with a muon signal in the BAC.

To select events offline containing exclusively produced $J/\psi(1S)$ or $\psi(2S)$ vector mesons in photoproduction, the following additional requirements were imposed:

- the Z coordinate of the event vertex reconstructed from the tracks was required to be within $\pm 30\,\text{cm}$ of the nominal ep interaction point and the transverse distance of the event vertex from the nominal ep interaction point was required to be within $0.03\,\text{cm}$;

- events with an identified electron with energy above $5\,\text{GeV}$, as reconstructed using an algorithm based on a neural network [29], were rejected. This removed DIS events with $Q^2 > 1\,\text{GeV}^2$;

- the sum of energy in the FCAL cells immediately surrounding the beam-pipe hole ($\theta < 0.12\,\text{rad}$) had to be smaller than $1\,\text{GeV}$ to suppress contamination from proton-dissociative events;

- the photon–proton centre-of-mass energy was required to be in the range $30 < W < 180\,\text{GeV}$, where W is reconstructed from the initial proton-beam energy, E_p, and the difference in energy and Z component of momentum, p_Z, of the vector-meson candidate, V, as $W = \sqrt{2E_p(E - p_Z)_V}$;

- the squared four-momentum transfer at the proton vertex was required to be in the range $|t| < 1\,\text{GeV}^2$, where t is reconstructed from the transverse momentum of the vector meson, $p_{T,V}$, as $t = -(p_{T,V})^2$. This requirement significantly reduced the remaining fraction of proton-dissociative events;

- each track considered was required to produce hits in the first CTD superlayer or in the MVD and cross at least three CTD superlayers. These requirements effectively limit the pseudorapidity range of each track to $-1.9 < \eta < 1.9$ and ensured the selection of tracks with good momentum resolution;

- two oppositely-charged tracks, each with $p_T > 1\,\text{GeV}$, matched to the vertex were required in the event. Each of these tracks was matched with a cluster in the CAL. The cluster was required to be consistent with a muon identified with an algorithm based on a neural network [30]. At least one of these tracks had to be associated with a F/B/RMUON signal or with a muon signal in the BAC found using the GMUON algorithm with muon quality ≥ 1 [31];

- for the selection of $J/\psi(1S) \rightarrow \mu^+\mu^-$ and $\psi(2S) \rightarrow \mu^+\mu^-$ events, no additional tracks were allowed. Cosmic-ray events were rejected by requiring $t_{\mathrm{down}} - t_{\mathrm{up}} < 8\,\mathrm{ns}$, where t_{down} and t_{up} represent the calorimeter signal times in the lower and upper halves of the CAL. Additionally, $\cos\alpha > -0.985$ was required, where α is the angle between the momentum vectors of the candidate μ^+ and μ^-;
- for the selection of $\psi(2S) \rightarrow J/\psi(1S)\,\pi^+\pi^-$ events, exactly two additional oppositely-charged tracks were required. Their momenta were required to be lower than those of the muons. Each track was required to have a transverse momentum above 0.12 GeV. No explicit vertex association was required for these two tracks;
- the energy of any additional CAL cluster not associated with a muon candidate, or with a pion candidate in the case of $\psi(2S) \rightarrow J/\psi(1S)\,\pi^+\pi^-$ events, was required to be less than 0.5 GeV. This ensured that events with other produced neutral particles were rejected while events with clusters in the CAL consistent with noise only were not rejected.

After rejection of DIS events, a study of generator-level events from the DIFFVM MC sample yielded a median Q^2 of about $3 \times 10^{-5}\,\mathrm{GeV}^2$. A similar study showed that 99% of proton-dissociative events remaining after the above requirements had a diffractive mass $M_Y \lesssim 5\,\mathrm{GeV}$.

4.2 Signal extraction

In the following, the signal extraction for the $\mu^+\mu^-$ and $\mu^+\mu^-\pi^+\pi^-$ final states are discussed separately.

Figure 2 shows the $\mu^+\mu^-$ mass distributions between 2 and 6 GeV for the selected events in the full region, $30 < W < 180\,\mathrm{GeV}$, and in W intervals within this full range in which the cross section is measured. Figure 3 shows the $\mu^+\mu^-$ mass distribution in the full region, $0.0 < |t| < 1.0\,\mathrm{GeV}^2$, and in $|t|$ intervals within this full range in which the cross section is measured. Clear $J/\psi(1S)$ and $\psi(2S)$ peaks are seen and no other significant peak is observed.

Expectations from MC simulations are also shown in Figs. 2 and 3, where here and in all subsequent figures showing MC simulations, the sum of all the MC distributions is normalised to data. The relative contribution of each different process was obtained from a fit to the data in the range $2 < M(\mu^+\mu^-) < 6\,\mathrm{GeV}$. The $J/\psi(1S)$ and $\psi(2S)$ peaks in all W and $|t|$ ranges are consistent with events from elastic and proton-dissociative processes. The varying width of the peak with increasing W is due to the different amount of tracking information available; low W and high W corresponds to muons in the forward and rear directions respectively where the resolution is less good than in the central tracking region, i.e. $60 < W < 120\,\text{GeV}$. The different $M(\mu^+\mu^-)$ resolutions with W are reproduced well by the detector MC simulation. The distributions outside of the $J/\psi(1S)$ and $\psi(2S)$ peaks are, according to MC simulations, consistent with those arising from the Bethe–Heitler process. The width of the peak does not change with varying $|t|$ because $|t|$ is not correlated with the angular distribution of the muons. However, the Bethe–Heitler background decreases significantly with increasing $|t|$.

The numbers of $J/\psi(1S)$ and $\psi(2S)$ mesons were obtained from a fit to the data to describe the peaks and the background. Each of the peaks was fitted using the sum of two Gaussian functions centred at the same (common) mean value. The fit was further constrained by imposing the same ratios of the widths (sigmas) and the normalisations for the two Gaussian shapes describing the $J/\psi(1S)$ and $\psi(2S)$ peaks. This was motivated by the observed scaling of the mass resolution with increasing mass of the resonance and stabilises the fit of the $\psi(2S)$ peak, which has lower statistics. The background function used was $F(x) = A(x - B)^C \cdot \exp(-D[x - B] - E[x - B]^2)$ where $x = M(\mu^+\mu^-)$, A, C D and E are parameters determined in the fit and B represents the kinematic onset of the distribution and is fixed to $2\,\text{GeV}$, twice the minimum p_T of a muon. The results of these fits are also shown in Figs. 2 and 3 where they describe the data well. A resonant background in the $J/\psi(1S)$ peak from the decay of $\psi(2S)$ mesons where the other decay products are not reconstructed is also shown as part of the $\psi(2S)$ MC distribution; this was estimated to be about 2.4% and will later be subtracted from the Gaussian fit. The non-resonant background under the $J/\psi(1S)$ peak from the Bethe–Heitler process is on average about 9% of the size of the signal. Under the $\psi(2S)$ peak, the background from the Bethe–Heitler process is about a factor of 2.5 times higher than the signal. A resonant background under the $\psi(2S)$ peak arises due to leakage from the reconstruction of J/ψ mesons, the upper tail of which overlaps with the $\psi(2S)$ mass region. It is on average 15% of the $\psi(2S)$ signal.

Figure 4 shows the $\mu^+\mu^-\pi^+\pi^-$ mass distribution between 3.4 and 4 GeV and the difference in masses, $M(\mu^+\mu^-\pi^+\pi^-) - M(\mu^+\mu^-)$, for the selected events, with the additional requirements of $2.8 < M(\mu^+\mu^-) < 3.4\,\text{GeV}$ and $0.5 < M(\mu^+\mu^-\pi^+\pi^-) - M(\mu^+\mu^-) < 0.7\,\text{GeV}$. Clear, narrow peaks are observed in both distributions, especially for the mass difference, and both are described well by MC simulations. The distributions are consistent with events from elastic and proton-dissociative processes with a small non-resonant background that is about $2 - 3\%$ of the signal size. The number of background events in the $\psi(2S) \to \mu^+\mu^-\pi^+\pi^-$ sample was estimated from data by counting the side-band events in the $M(\mu^+\mu^-\pi^+\pi^-) - M(\mu^+\mu^-)$ distribution outside the signal region, before applying the cut on this quantity. The background events were counted in the $0.7 - 1.5\,\text{GeV}$ interval and the obtained number was rescaled to the signal interval $0.5 - 0.7\,\text{GeV}$ (see Fig. 4(b)) assuming a uniform distribution. Such a procedure was performed for each W and $|t|$ interval. The number of $\psi(2S)$ mesons was found by counting the number of entries and subtracting the background in the range $3.4 < M(\mu^+\mu^-\pi^+\pi^-) < 4\,\mathrm{GeV}$.

The numbers of signal and background events and their statistical uncertainties used for further analysis are given in Table 1 for each channel and in five W and five $|t|$ regions.

4.3 Correction procedure and comparison of measured and simulated distributions

In order to determine the acceptance using simulated events, simulated and measured distributions have to agree. To achieve this, corrections for the efficiency of muon reconstruction were developed for the MC simulation. Muon-identification corrections were developed using a sample of exclusive dimuon events in which one muon was tagged and the probability of reconstruction of the other muon evaluated. The probability was determined for the full reconstruction chain, including the trigger efficiency, in bins of η^μ and $p_Z^\mu/p_T^\mu/p^\mu$, depending on whether the muon was reconstructed in the R/B/FMUON. This leads to typical efficiencies of $20-40\%$, averaged over η^μ and momentum, although in individual bins of η^μ and $p_Z^\mu/p_T^\mu/p^\mu$ these can be under 10%, mainly at low momentum where the muons do not reach the detectors. They can reach up to 60% at high p_Z^μ and high p_T^μ. The efficiency to reconstruct muons in the CAL was typically above 90%. After application of the data-driven corrections, the data and MC distributions agree well.

The CTD first-level trigger used in the selection of events has an efficiency that depends on the track multiplicity and needs to be evaluated for the $\mu^+\mu^-\pi^+\pi^-$ final state with an independent trigger. A sample of DIS events [1], passing an independent trigger chain but with the same final state, was used to determine this correction. To ensure the same tracking topology, the scattered electron was restricted to the RCAL cells close the beam-pipe with no matched track. This correction was consistent with unity to within about $\pm 5\%$.

The tracking efficiency for low-momentum pions ($p_T < 0.26\,\mathrm{GeV}$) is overestimated in MC simulations and so a correction was applied [32, 33] in simulations to $\psi(2S)$ decays to $\mu^+\mu^-\pi^+\pi^-$. An event was assigned a weight given by $w = 1 + 0.548 \cdot (p_T^\pi - 0.26)$ if one pion had transverse momentum, p_T^π, below $0.26\,\mathrm{GeV}$. If both pions had transverse momentum below $0.26\,\mathrm{GeV}$, the quantity w was calculated for each pion and the event weighted by the product of the two weights.

Data and MC simulations with a $\mu^+\mu^-$ pair are compared in Fig. 5 for $2.8 < M(\mu^+\mu^-) < 3.4\,\mathrm{GeV}$ and $3.4 < M(\mu^+\mu^-) < 4.0\,\mathrm{GeV}$, corresponding to the mass ranges of the $J/\psi(1S)$

and $\psi(2S)$, respectively, after application of all corrections discussed above. The structures in the W data distribution reflect the acceptance of the detector, in particular that of the muon detectors, with the dips around 80 GeV due to the cuts to remove cosmic-ray events. The data distributions are well described by MC simulations. This demonstrates the validity of the correction procedure for the muon acceptance and tuning of the MC simulation parameters. The data distribution in $|t|$ exhibits an exponential fall-off with increasing $|t|$ and is well described by the mixture of MC samples. The fraction of proton-dissociative events increases significantly with increasing $|t|$, becoming the dominant process above $1\,\text{GeV}^2$; this justifies the requirement in the analysis of $|t| < 1\,\text{GeV}^2$ in order to enrich the sample in elastic events.

Figure 6 shows distributions in W and $|t|$ when $\mu^+\mu^-\pi^+\pi^-$ were observed in the final state. The W distribution is reasonably flat in the range $40 < W < 150\,\text{GeV}$ with fall-offs either side of this region. The $|t|$ distribution exhibits an exponential fall-off with increasing $|t|$. The MC simulations give a reasonable description of the data.

5 Cross-section ratio $\psi(2S)$ to $J/\psi(1S)$

The following cross-section ratios, $\sigma_{\psi(2S)}/\sigma_{J/\psi(1S)}$, have been measured: $R_{\mu\mu}$ for $\psi(2S) \to \mu^+\mu^-$, $R_{J/\psi\,\pi\pi}$ for $\psi(2S) \to J/\psi(1S)\,\pi^+\pi^-$ and R for the combination of the two decay modes. In each case, the decay $J/\psi(1S) \to \mu^+\mu^-$ was used in the denominator.

5.1 Determination of the cross-section ratio

The cross-section ratios for each bin and the full sample were calculated using

$$R_{\mu\mu} = \left[\left(\frac{N_{\mu\mu}^{\psi(2S)}}{B_{\psi(2S)\to\mu^+\mu^-} \cdot A_{\mu\mu}^{\psi(2S)}} \right) \Big/ \left(\frac{N_{\mu\mu}^{J/\psi(1S)}}{B_{J/\psi(1S)\to\mu^+\mu^-} \cdot A_{\mu\mu}^{J/\psi(1S)}} \right) \right] \cdot \frac{1 - f_{\text{pdiss}}^{\psi(2S)}}{1 - f_{\text{pdiss}}^{J/\psi(1S)}}$$

and

$$R_{J/\psi\,\pi\pi} = \left[\left(\frac{N_{J/\psi\,\pi\pi}^{\psi(2S)}}{B_{\psi(2S)\to J/\psi(1S)\,\pi^+\pi^-} \cdot A_{J/\psi\,\pi\pi}^{\psi(2S)}} \right) \Big/ \left(\frac{N_{\mu\mu}^{J/\psi(1S)}}{A_{\mu\mu}^{J/\psi(1S)}} \right) \right] \cdot \frac{1 - f_{\text{pdiss}}^{\psi(2S)}}{1 - f_{\text{pdiss}}^{J/\psi(1S)}} \,.$$

Here N_i^j denotes the number of observed signal events for the charmonium state j with the decay mode i, A_i^j is the corresponding acceptance determined from the ratio of reconstructed to generated MC events after reweighting, and f_{pdiss}^j is the fraction of proton-dissociative events. The value of $f^{j}_{\rm pdiss}$ was determined by fitting the $|t|$ distribution, for $|t| < 6.25\,{\rm GeV}^2$, of the data with the $|t|$ distributions from MC samples. It was found that $f^{j}_{\rm pdiss}$ is independent of W and so the mean values of $f^{J/\psi(1S)}_{\rm pdiss} = 17\%$ and $f^{\psi(2S)}_{\rm pdiss} = 16\%$ were used for the determination of R as a function of W. The value of $f^{j}_{\rm pdiss}$ has a strong dependence on $|t|$, varying from about 7% for $0 < |t| < 0.1\,{\rm GeV}^2$ to 45% for $0.6 < |t| < 1\,{\rm GeV}^2$ (see Table 1 for more details). The corresponding values in each bin were used in the determination of R as a function of $|t|$. However, there is little difference between $f^{J/\psi(1S)}_{\rm pdiss}$ and $f^{\psi(2S)}_{\rm pdiss}$ and so the final factor in the calculation of $R_{\mu\mu}$ and $R_{J/\psi\,\pi\pi}$ is approximately unity. The following values were used for the branching fractions: $B_{J/\psi(1S)\to\mu^+\mu^-} = (5.961 \pm 0.033)\%$, $B_{\psi(2S)\to\mu^+\mu^-} = (0.80 \pm 0.06)\%$ and $B_{\psi(2S)\to\mu^+\mu^-\pi^+\pi^-} = (2.07 \pm 0.02)\%$ [34].

The cross-section ratios for the two decay channels, $R_{\mu\mu}$ for $\psi(2S) \to \mu^+\mu^-$ and $R_{J/\psi\,\pi\pi}$ for $\psi(2S) \to J/\psi(1S)\,\pi^+\pi^-$ are shown in Fig. 7 in bins of W and $|t|$, with statistical uncertainties only. The values are consistent for the two channels. The two independent measurements of the cross-section ratio $\sigma_{\psi(2S)}/\sigma_{J/\psi(1S)}$ were combined. The combined cross-section ratio, R, was obtained using the weighted average of the cross sections determined for the two $\psi(2S)$ decay modes. The statistical uncertainties were used for the weights. The combined cross-section ratio, R, is also shown in Fig. 7, with statistical uncertainties only.

5.2 Systematic uncertainties

The systematic uncertainties on the R values were obtained by performing a suitable variation to determine the change of R relative to its central value for each source of uncertainty. The following sources of systematic uncertainty were considered, with typical values given for the change on the final measured R value:

- the t dependence ($\exp(-b|t|)$) of the DIFFVM MC simulations was varied by the uncertainty on the b values: $4.6 \pm 0.3\,{\rm GeV}^{-2}$ and $4.3 \pm 0.7\,{\rm GeV}^{-2}$ for $J/\psi(1S)$ and $\psi(2S)$ elastic events and $1.0 \pm 0.1\,{\rm GeV}^{-2}$ and $0.7 \pm 0.2\,{\rm GeV}^{-2}$ for $J/\psi(1S)$ and $\psi(2S)$ proton-dissociative events. Additionally, the α' parameter in the re-weighting of b was varied by its uncertainty, $\alpha' = 0.12 \pm 0.04\,{\rm GeV}^{-2}$. The variation in b for $\psi(2S)$ proton-dissociative events led to changes in R that increased with increasing $|t|$, with an average change of ± 0.01 in R. The other variations led to typical changes of below ± 0.005 in R;

- the W dependence (W^{δ}) of the DIFFVM MC simulations was varied by the uncertainty on δ values: 0.67 ± 0.10 and 1.10 ± 0.20 for $J/\psi(1S)$ and $\psi(2S)$ elastic events and 0.42 ± 0.15 and 0.70 ± 0.30 for $J/\psi(1S)$ and $\psi(2S)$ proton-dissociative events. Typical variations were ± 0.001 in R;

- the M_Y dependence ($1/M_Y^{\beta}$) of the DIFFVM MC simulations was varied by an uncertainty on β, 2.4 ± 0.3, estimated from comparisons to previous H1 and ZEUS analyses. These variations led to a change of less than ± 0.001 in R;

- the correction factors determined in η^{μ} and $p_Z^{\mu}/p_T^{\mu}/p^{\mu}$ bins for the muon efficiencies were varied by doubling the bin size in the η^{μ} and $p_Z^{\mu}/p_T^{\mu}/p^{\mu}$ grid. These variations led to a change of -0.001 in R;

- the minimum muon-p_T cut was varied from 1.0 GeV by ± 0.1 GeV to check the stability of the background estimation from the fit at the lower edge of the dimuon mass spectrum and led to a change of $^{+0.002}_{-0.000}$ in R;

- the minimum pion-p_T cut was varied from 0.12 GeV by ± 0.02 GeV, where the value 0.1 GeV is consistent with the lower edge of the tracker acceptance, and led to a change of $^{+0.003}_{-0.001}$ in R;

- the pion-candidate tracks in the $\psi(2S) \to \mu^+\mu^-\pi^+\pi^-$ decay were required to be associated to the vertex rather than the default of no vertex requirement. This led to a change of -0.007 in R;

- the transverse-momentum cut for the correction of pion-candidate tracks was varied from 0.26 GeV by ± 0.04 GeV and led to a change of $^{+0.002}_{-0.001}$ in R;

- the maximum energy of a CAL cluster not associated with a muon or pion candidate was varied from the default 0.5 GeV by ± 0.1 GeV [1] and led to a change of $^{+0.002}_{-0.004}$ in R;

- the maximum energy inside a cone of maximum angle surrounding the FCAL beampipe hole used to suppress proton-dissociative events were varied from the defaults: $\theta = 0.12 \pm 0.02$ rad and energy of 1.00 ± 0.25 GeV. All variations led to a change of less than ± 0.001 in R;

- the cut on the timing difference in the CAL, $t_{\rm down} - t_{\rm up}$ was varied from the default 8 ns by ± 1 ns, according to a study of cosmic-ray muons, and led to a change of less than $^{+0.002}_{-0.000}$ in R;

- the numbers of $J/\psi(1S)$ and $\psi(2S)$ mesons were extracted using a MC template fit, rather than the two Gaussian and background functions, as a check of modelling the background (see Figs. 2 and 3), and led to a change of -0.010 in R;

- the branching ratios were varied according to their uncertainties given in Section 5.1 and led to changes of ±0.001, ∓ 0.007 and less than ∓ 0.001 in R for the variations in $B_{J/\psi(1S)\to\mu^+\mu^-}$, $B_{\psi(2S)\to\mu^+\mu^-}$ and $B_{\psi(2S)\to\mu^+\mu^-\pi^+\pi^-}$, respectively.

The largest uncertainties arose from the change in the b slope, especially for $\psi(2S)$ proton-dissociative events and especially at high $|t|$, the vertexing of the pion-candidate tracks, the method for extracting the number of signal events, and the branching ratio $B_{\psi(2S)\to\mu^+\mu^-}$. The total systematic uncertainty, given in Table 1, was obtained from the separate quadratic sums of the positive and negative changes in each bin.

A steepening of the $|t|$ distribution to low M_Y has been observed in hadron–hadron diffraction [35, 36]. To investigate this possibility in photoproduction, the b values in the MC simulation for the proton-dissociative events were changed to those extracted from elastic events, i.e. from 1.0 to 4.6 GeV^{-2} for $J/\psi(1S)$ and from 0.7 to 4.3 GeV^{-2} for $\psi(2S)$ events for $M_Y < 1.9\,\text{GeV}$. This led to an average change of -0.009 in R with a change of -0.005 at lowest $|t|$ and -0.015 at highest $|t|$. This was not included in the total systematic uncertainty as such a change led to a poor description of the forward energy flow, estimated by the sum of energy in the FCAL surrounding the beam-pipe hole ($\theta < 0.12\,\text{rad}$).

6 Results

The cross-section ratio $R = \sigma_{\psi(2S)}/\sigma_{J/\psi(1S)}$ has been measured in exclusive photoproduction in the kinematic range $Q^2 < 1\,\text{GeV}^2$, $30 < W < 180\,\text{GeV}$ and $|t| < 1\,\text{GeV}^2$ using a total integrated luminosity of 373 pb^{-1}. The measured value is

$$R = 0.146 \pm 0.010\,(\text{stat.})\,^{+0.016}_{-0.020}\,(\text{syst.})\,,$$

where the first uncertainty is statistical and the second is the sum of all systematic uncertainties added in quadrature. This value, well below 1, confirms the expected suppression of the $\psi(2S)$ cross section relative to the $J/\psi(1S)$ cross section.

The cross-section ratios differential in W and $|t|$ are shown in Fig. 8 and given in Table 1. As a function of W, the value of R is compatible with a constant value. A slow increase of R with increasing $|t|$ is observed. The measurements presented in Fig. 8(a) are in agreement with previous measurements from H1 [3,4]. In DIS [1] neither a W dependence nor a $|t|$ dependence of R was observed. A discussion of the comparison of the results to various model predictions is presented in Section 7.

The value of R given above is shown in Fig. 9 compared with other measurements in photoproduction and measurements in DIS as a function of Q^2. The value measured here confirms the previous measurements in photoproduction [3, 4]. The trend of decreasing R with decreasing Q^2 down to $\approx 0\,\mathrm{GeV}^2$ is also confirmed.

7 Comparison to model predictions

Several models of exclusive vector-meson production are available and also predict the ratio of the production of $\psi(2S)$ to $J/\psi(1S)$ mesons. Predictions from three different models were compared to the data and are briefly described. All models predictions were calculated for the kinematic region $30 < W < 180\,\mathrm{GeV}$ and $|t| < 1\,\mathrm{GeV}^2$.

7.1 Individual models

The model from Bendová, Čepila and Contreras [37] (BCC hot-spots) is based on energy-dependent hot spots, i.e. regions of high gluon density in the proton. The slope parameter $b = 4.7\,\mathrm{GeV}^{-2}$ was used for both $J/\psi(1S)$ and $\psi(2S)$ production. The b value was derived from H1 and ZEUS data on $J/\psi(1S)$ photoproduction.

The model from Nemchik et al. [38–40] (JN) provides predictions with various combinations of colour-dipole interactions, skewness parameters in the gluon density and quarkonia potentials used for the calculation of the centre-of-mass wave functions. The predictions shown are based on the Golec-Biernat–Wüsthoff (GBW) colour-dipole model [41,42] with skewness. The phenomenological quarkonia potentials used were: the so-called Buchmüller–Tye (BT), logarithmic (Log), Cornell (Cor) and power-law (Pow). Other combinations of colour-dipole models with or without skewness differ to those shown by 5–10%.

Lappi and Mäntysaari [43] (LM) use the BFKL evolution as well as the IP-Sat model [44] to predict vector-meson production in ep and electron–ion collisions in the dipole picture. The wave functions of the $J/\psi(1S)$ and $\psi(2S)$ have been calculated according to the boosted Gaussian (BG) procedure [45, 46] and the low-x inclusive HERA data have been used to constrain the $c\bar{c}$–dipole cross section.

7.2 Comparison of models and data

In Fig. 8, model predictions are compared to photoproduction data as a function of W and $|t|$. All model predictions exhibit a mild rise in R with increasing W. The predicted rise is similar for all models. The absolute values of the predictions differ by up to a factor of 2. The predictions from BCC lie above the data and the predictions from LM lie below the data. No uncertainties for these predictions are provided. The shapes of the models are consistent with the data, although the data are also consistent with no increase with W. The predictions from JN give a better description of the normalisation and the differences in predictions due to the quarkonia potential also give some indication of the uncertainty in the models.

All models also predict an increase in R with increasing $|t|$, and again predict similar gradients but different absolute values. Given the uncertainties in the data and the spread of the models, the description of the data is good.

In Fig. 9, model predictions are compared to photoproduction and DIS data as a function of Q^2. All models predict a strong increase in R with increasing Q^2, which is compatible with the trend seen in the data. Towards higher Q^2, the LM and BCC models exhibit a flattening of R compared to the JN models. The photoproduction data have the potential to constrain the models further.

Overall, the predictions from the three models, BCC, JN and LM, give a reasonable description of the W, $|t|$ and Q^2 dependence of R.

8 Summary

The cross-section ratio $R = \sigma_{\psi(2S)}/\sigma_{J/\psi(1S)}$ in exclusive photoproduction has been measured with the ZEUS detector at HERA in the kinematic range $Q^2 < 1\,\text{GeV}^2$, $30 < W < 180\,\text{GeV}$ and $|t| < 1\,\text{GeV}^2$, using an integrated luminosity of $373\,\text{pb}^{-1}$. The decay channels used were $\mu^+\mu^-$ and $J/\psi(1S)\,\pi^+\pi^-$ for the $\psi(2S)$ and $\mu^+\mu^-$ for the $J/\psi(1S)$. The cross-section ratio was determined as a function of W and $|t|$ and presented as a function of Q^2. As a function of W, the value of R is compatible with a constant value. A slow increase of R with increasing $|t|$ is observed. The data confirm previous conclusions that R decreases with decreasing Q^2. Three model calculations were compared to the measured dependences of R and give a reasonable description of the data, which can be used to constrain the models further.

Acknowledgements

We appreciate the contributions to the construction, maintenance and operation of the ZEUS detector of many people who are not listed as authors. The HERA machine group and the DESY computing staff are especially acknowledged for their success in providing excellent operation of the collider and the data-analysis environment. We thank the DESY directorate for their strong support and encouragement. We thank Dagmar Bendová, Jan Čepila, Michal Křelina, Jan Nemchik and Heikki Mäntysaari for providing model predictions and for useful discussions.

References

[1] ZEUS Coll., H. Abramowicz et al., Nucl. Phys. **B 909**, 934 (2016).

[2] H1 Coll., C. Adloff et al., Eur. Phys. J. **C 10**, 373 (1999).

[3] H1 Coll., C. Adloff et al., Phys. Lett. **B 541**, 251 (2002).

[4] H1 Coll., C. Adloff et al., Phys. Lett. **B 421**, 385 (1998).

[5] ZEUS Coll., U. Holm (ed.), *The ZEUS Detector,* Status Report, DESY (1993), doi:10.3204/PUBDB-2017-12635. `http://www-zeus.desy.de/bluebook/bluebook.html`.

[6] N. Harnew et al., Nucl. Inst. Meth. **A 279**, 290 (1989).

[7] B. Foster et al., Nucl. Phys. Proc. Suppl. **B 32**, 181 (1993).

[8] B. Foster et al., Nucl. Inst. Meth. **A 338**, 254 (1994).

[9] A. Polini et al., Nucl. Inst. Meth. **A 581**, 656 (2007).

[10] M. Derrick et al., Nucl. Inst. Meth. **A 309**, 77 (1991).

[11] A. Andresen et al., Nucl. Inst. Meth. **A 309**, 101 (1991).

[12] A. Caldwell et al., Nucl. Inst. Meth. **A 321**, 356 (1992).

[13] A. Bernstein et al., Nucl. Inst. Meth. **A 336**, 23 (1993).

[14] I. Kudla et al., Nucl. Inst. Meth. **A 300**, 480 (1991).

[15] J. Andruszków et al., Preprint DESY–92–066, DESY (1992).

[16] ZEUS Coll., M. Derrick et al., Z. Phys. **C 63**, 391 (1994).

[17] J. Andruszków et al., Acta Phys. Polon. **B 32**, 2025 (2001).

[18] M. Helbich et al., Nucl. Inst. Meth. **A 565**, 572 (2006).

[19] L. Adamczyk et al., Nucl. Inst. and Meth. **A 744**, 80 (2014).

[20] B. List and A. Mastroberardino, *Proc. Workshop on Monte Carlo Generators for HERA Physics*, A.T. Doyle, G. Grindhammer, G. Ingelman, H. Jung (eds.), p. 396, DESY, Hamburg, Germany (1999). Also in preprint DESY-PROC-1999-02.

[21] H1 Coll., C. Alexa et al., Eur. Phys. J. **C 73**, 2466 (2013).

[22] A. Levy, *Proc. 14th Topical Conference, HCP 2002*, M. Erdmann and T. Muller (eds.), p.173, Karlsruhe, Germany (2002). Also in preprint hep-ex/0301022.

[23] ZEUS Coll., S. Chekanov et al., Eur. Phys. J. **C 24**, 345 (2002).

[24] T.N. Pham, B. Pire and T.N. Truong, Phys. Lett. **B 61**, 183 (1976).

[25] T. Abe, Comp. Phys. Comm. **136**, 126 (2001).

[26] R. Brun et al., GEANT3, Technical Report CERN-DD/EE/84-1, CERN, 1987.

[27] P.D. Allfrey et al., Nucl. Inst. Meth. **A 580**, 1257 (2007).

[28] W.H. Smith, K. Tokushuku and L.W. Wiggers, *Proc. Computing in High-Energy Physics (CHEP), Annecy, France, Sept. 1992*, C. Verkerk and W. Wojcik (eds.), p. 222. CERN, Geneva, Switzerland (1992). Also in preprint DESY–92–150B.

[29] H. Abramowicz, A. Caldwell and R. Sinkus, Nucl. Inst. Meth. **A 365**, 508 (1995).

[30] V.A. Kuzmin, Nucl. Inst. Meth. **A 453**, 336 (2000).

[31] I. Bloch, Ph.D. Thesis, Hamburg University, Report DESY-THESIS-2005-034 (2005).

[32] V. Libov, Ph.D. Thesis, Hamburg University, Report DESY-THESIS-2013-030 (2013).

[33] O. Bachynska, Ph.D. Thesis, Hamburg University, Report DESY-THESIS-2012-045 (2012).

[34] P.A. Zyla et al., Prog. Theor. Exp. Phys. **2020**, 083C01 (2020).

[35] Y. Akimov et al., Phys. Rev. **D 14**, 3148 (1976).

[36] M. Albrow et al., Nucl. Phys. **B 108**, 1 (1976).

[37] D. Bendova, J. Cepila and J.G. Contreras, Phys. Rev. **D 99**, 034025 (2019).

[38] M. Krelina et al., Eur. Phys. J. **C 79**, 154 (2019).

[39] J. Cepila et al., Eur. Phys. J. **C 79**, 495 (2019).

[40] B.Z. Kopeliovich, M. Krelina and J. Nemchik, Phys. Rev. **D 103**, 094027 (2021).

[41] K.J. Golec-Biernat and M. Wusthoff, Phys. Rev. **D 59**, 014017 (1998).

[42] K.J. Golec-Biernat and M. Wusthoff, Phys. Rev. **D 60**, 114023 (1999).

[43] T. Lappi and H. Mäntysaari, Phys. Rev. **C 83**, 065202 (2011).

[44] A.H. Reazeian et al., Phys. Rev. **D 87**, 034002 (2013).

[45] T. Lappi and H. Mäntysaari, PoS (DIS2014), 069 (2014).

[46] H. Kowalski, L. Motyka and G. Watt, Phys. Rev. **D 74**, 074016 (2006).

bin	channel	$\langle W \rangle, \langle t \rangle$	signal	bg-nonres	bg-res	A	$f_{\rm pdiss}$	$\langle f^{\psi(2S)}_{\rm pdiss} \rangle$	$R_{\mu\mu},\ R_{J/\psi\,\pi\pi}$	R
All	$J/\psi(1S) \to \mu^+\mu^-$	91.4, 0.219	23043 ± 169	2106 ± 46	550 ± 40	0.090 ± 0.0003	0.168 ± 0.004			0.146
events	$\psi(2S) \to \mu^+\mu^-$	95.8, 0.223	690 ± 50	1701 ± 41	103 ± 10	0.132 ± 0.0008	0.15 ± 0.02	0.16 ± 0.01	0.154 ± 0.012	±0.010 (stat.)
	$\psi(2S) \to \mu^+\mu^-\pi^+\pi^-$	99.6, 0.225	387 ± 20	10 ± 3		0.035 ± 0.0050	0.18 ± 0.02		0.125 ± 0.019	$^{+0.016}_{-0.020}$ (syst.)
W1	$J/\psi(1S) \to \mu^+\mu^-$	45.5	7301 ± 104	677 ± 26	148 ± 27	0.087 ± 0.0006	0.168 ± 0.004			0.128
(30,60)	$\psi(2S) \to \mu^+\mu^-$	48.1	178 ± 33	500 ± 22	38 ± 6	0.115 ± 0.0014	0.15 ± 0.02	0.16 ± 0.01	0.138 ± 0.025	±0.017 (stat.)
GeV	$\psi(2S) \to \mu^+\mu^-\pi^+\pi^-$	50.7	68 ± 8	1.0 ± 1.0		0.020 ± 0.0030	0.18 ± 0.02		0.120 ± 0.024	$^{+0.013}_{-0.025}$ (syst.)
W2	$J/\psi(1S) \to \mu^+\mu^-$	74.6	3985 ± 80	342 ± 18	136 ± 17	0.072 ± 0.0006	0.168 ± 0.004			0.123
(60,90)	$\psi(2S) \to \mu^+\mu^-$	73.9	123 ± 16	404 ± 20	1 ± 1	0.121 ± 0.0016	0.15 ± 0.02	0.16 ± 0.01	0.137 ± 0.018	±0.013 (stat.)
GeV	$\psi(2S) \to \mu^+\mu^-\pi^+\pi^-$	75.2	87 ± 10	3.8 ± 2.0		0.043 ± 0.0065	0.18 ± 0.02		0.105 ± 0.020	$^{+0.015}_{-0.016}$ (syst.)
W3	$J/\psi(1S) \to \mu^+\mu^-$	105.6	5278 ± 81	561 ± 24	164 ± 19	0.115 ± 0.0008	0.168 ± 0.004			0.164
(90,120)	$\psi(2S) \to \mu^+\mu^-$	105.3	183 ± 21	401 ± 20	3 ± 2	0.166 ± 0.0020	0.15 ± 0.02	0.16 ± 0.01	0.180 ± 0.021	±0.016 (stat.)
GeV	$\psi(2S) \to \mu^+\mu^-\pi^+\pi^-$	105.6	114 ± 11	2.5 ± 1.6		0.051 ± 0.0080	0.18 ± 0.02		0.140 ± 0.026	$^{+0.019}_{-0.022}$ (syst.)
W4	$J/\psi(1S) \to \mu^+\mu^-$	129.7	3333 ± 65	294 ± 17	60 ± 12	0.127 ± 0.0011	0.168 ± 0.004			0.123
(120,140)	$\psi(2S) \to \mu^+\mu^-$	129.4	70 ± 14	198 ± 14	11 ± 3	0.162 ± 0.0026	0.15 ± 0.02	0.16 ± 0.01	0.124 ± 0.025	±0.018 (stat.)
GeV	$\psi(2S) \to \mu^+\mu^-\pi^+\pi^-$	129.3	64 ± 8	1.6 ± 1.3		0.059 ± 0.0105	0.18 ± 0.02		0.121 ± 0.027	$^{+0.016}_{-0.018}$ (syst.)
W5	$J/\psi(1S) \to \mu^+\mu^-$	153.1	3261 ± 71	202 ± 14	49 ± 10	0.074 ± 0.0006	0.168 ± 0.004			0.174
(140,180)	$\psi(2S) \to \mu^+\mu^-$	155.4	127 ± 27	178 ± 13	54 ± 7	0.112 ± 0.0017	0.15 ± 0.02	0.16 ± 0.01	0.191 ± 0.041	±0.028 (stat.)
GeV	$\psi(2S) \to \mu^+\mu^-\pi^+\pi^-$	153.2	54 ± 7	1.0 ± 1.0		0.022 ± 0.0043	0.18 ± 0.02		0.159 ± 0.038	$^{+0.021}_{-0.021}$ (syst.)
t1	$J/\psi(1S) \to \mu^+\mu^-$	0.046	7949 ± 107	1481 ± 38	165 ± 30	0.092 ± 0.0005	0.079 ± 0.002			0.102
(0.0,0.1)	$\psi(2S) \to \mu^+\mu^-$	0.047	176 ± 33	1238 ± 35	25 ± 5	0.132 ± 0.0014	0.06 ± 0.01	0.07 ± 0.01	0.115 ± 0.021	±0.013 (stat.)
GeV^2	$\psi(2S) \to \mu^+\mu^-\pi^+\pi^-$	0.046	108 ± 11	2.8 ± 1.7		0.039 ± 0.0058	0.08 ± 0.01		0.094 ± 0.017	$^{+0.010}_{-0.011}$ (syst.)
t2	$J/\psi(1S) \to \mu^+\mu^-$	0.146	4997 ± 77	154 ± 12	109 ± 15	0.092 ± 0.0006	0.105 ± 0.002			0.133
(0.1,0.2)	$\psi(2S) \to \mu^+\mu^-$	0.147	134 ± 18	152 ± 12	16 ± 4	0.135 ± 0.0017	0.09 ± 0.01	0.10 ± 0.01	0.138 ± 0.019	±0.015 (stat.)
GeV^2	$\psi(2S) \to \mu^+\mu^-\pi^+\pi^-$	0.147	82 ± 9	2.4 ± 1.5		0.035 ± 0.0056	0.11 ± 0.01		0.125 ± 0.024	$^{+0.013}_{-0.018}$ (syst.)
t3	$J/\psi(1S) \to \mu^+\mu^-$	0.285	5239 ± 81	199 ± 14	143 ± 19	0.090 ± 0.0006	0.164 ± 0.003			0.155
(0.2,0.4)	$\psi(2S) \to \mu^+\mu^-$	0.286	159 ± 21	190 ± 14	24 ± 5	0.133 ± 0.0016	0.13 ± 0.02	0.15 ± 0.01	0.156 ± 0.021	±0.017 (stat.)
GeV^2	$\psi(2S) \to \mu^+\mu^-\pi^+\pi^-$	0.284	100 ± 10	2.7 ± 1.6		0.033 ± 0.0051	0.18 ± 0.02		0.154 ± 0.029	$^{+0.020}_{-0.016}$ (syst.)
t4	$J/\psi(1S) \to \mu^+\mu^-$	0.486	2588 ± 54	60 ± 8	62 ± 10	0.088 ± 0.0009	0.275 ± 0.006			0.169
(0.4,0.6)	$\psi(2S) \to \mu^+\mu^-$	0.486	102 ± 17	66 ± 8	15 ± 4	0.128 ± 0.0023	0.23 ± 0.03	0.26 ± 0.02	0.207 ± 0.035	±0.024 (stat.)
GeV^2	$\psi(2S) \to \mu^+\mu^-\pi^+\pi^-$	0.486	45 ± 7	0.5 ± 0.7		0.032 ± 0.0056	0.29 ± 0.03		0.138 ± 0.032	$^{+0.032}_{-0.038}$ (syst.)
t5	$J/\psi(1S) \to \mu^+\mu^-$	0.750	2459 ± 55	73 ± 9	76 ± 11	0.080 ± 0.0011	0.469 ± 0.010			0.204
(0.6,1.0)	$\psi(2S) \to \mu^+\mu^-$	0.748	121 ± 18	77 ± 9	23 ± 5	0.119 ± 0.0028	0.43 ± 0.06	0.45 ± 0.04	0.254 ± 0.043	±0.029 (stat.)
GeV^2	$\psi(2S) \to \mu^+\mu^-\pi^+\pi^-$	0.755	53 ± 7	1.5 ± 1.2		0.031 ± 0.0055	0.47 ± 0.06		0.163 ± 0.039	$^{+0.070}_{-0.071}$ (syst.)

Table 1: *Table of results with columns showing the W and $|t|$ bins, the decay channel, the mean values, $\langle W \rangle$ and $\langle t \rangle$, the number of signal events, the number of background events from Bethe–Heitler events and combinatorial non-resonant background (bg-nonres) and resonant background, described in Section 4.2 (bg-res), the acceptance (A), the fraction of proton-dissociative events ($f_{\rm pdiss}$), the average fraction of events from proton dissociation for the two $\psi(2S)$ decay channels ($\langle f^{\psi(2S)}_{\rm pdiss} \rangle$), the cross-section ratios for $R_{\mu\mu}$ for $\psi(2S) \to \mu^+\mu^-$, $R_{J/\psi\,\pi\pi}$ for $\psi(2S) \to J/\psi(1S)\,\pi^+\pi^-$ and R for the combination of the two decay modes. Statistical and systematic uncertainties are given separately for R; all other uncertainties are statistical only.*

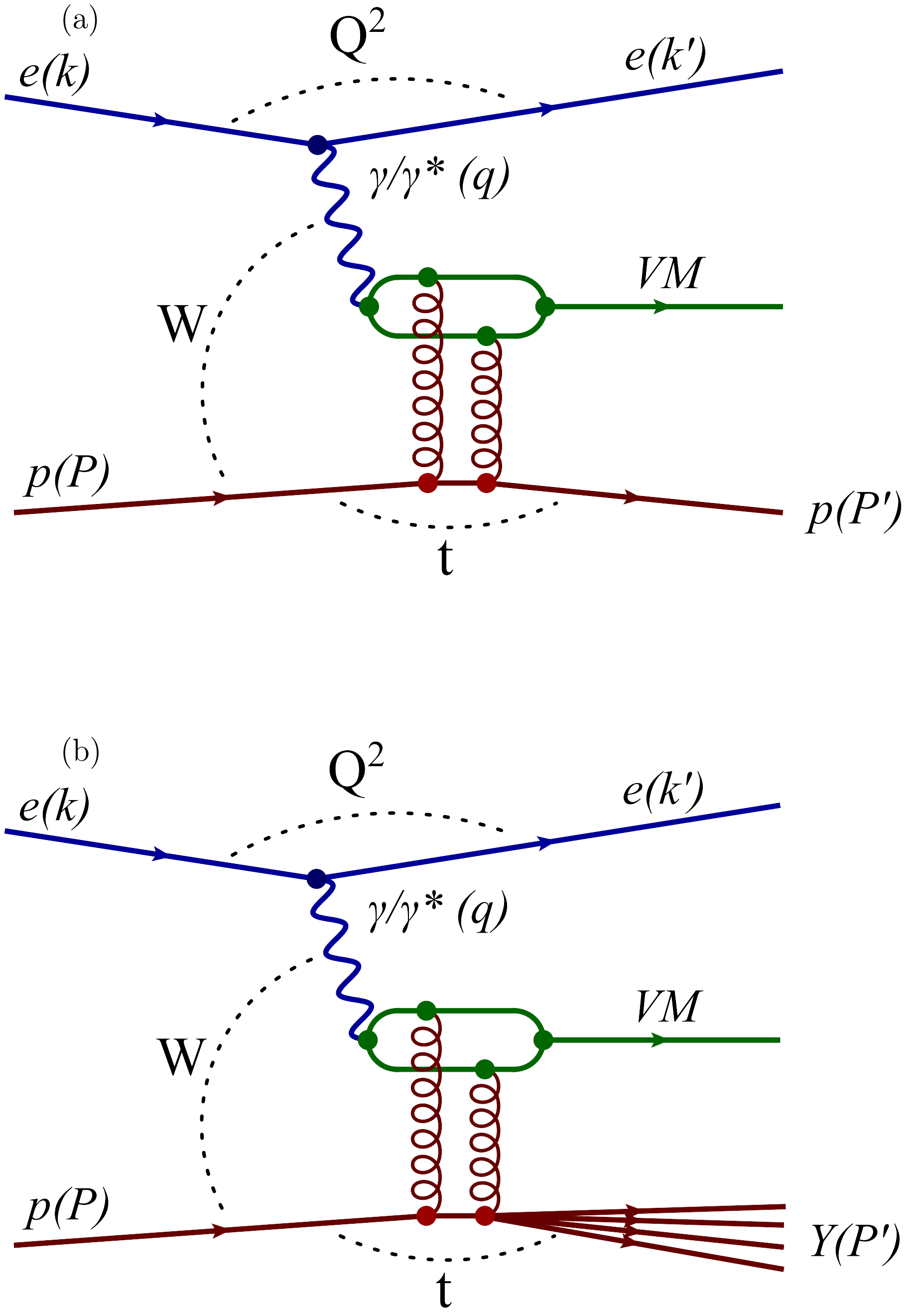

Figure 1: *Schematic representation of (a) exclusive and (b) proton-dissociative vector-meson production in ep scattering. For a description of the kinematic variables, see Section 1.*

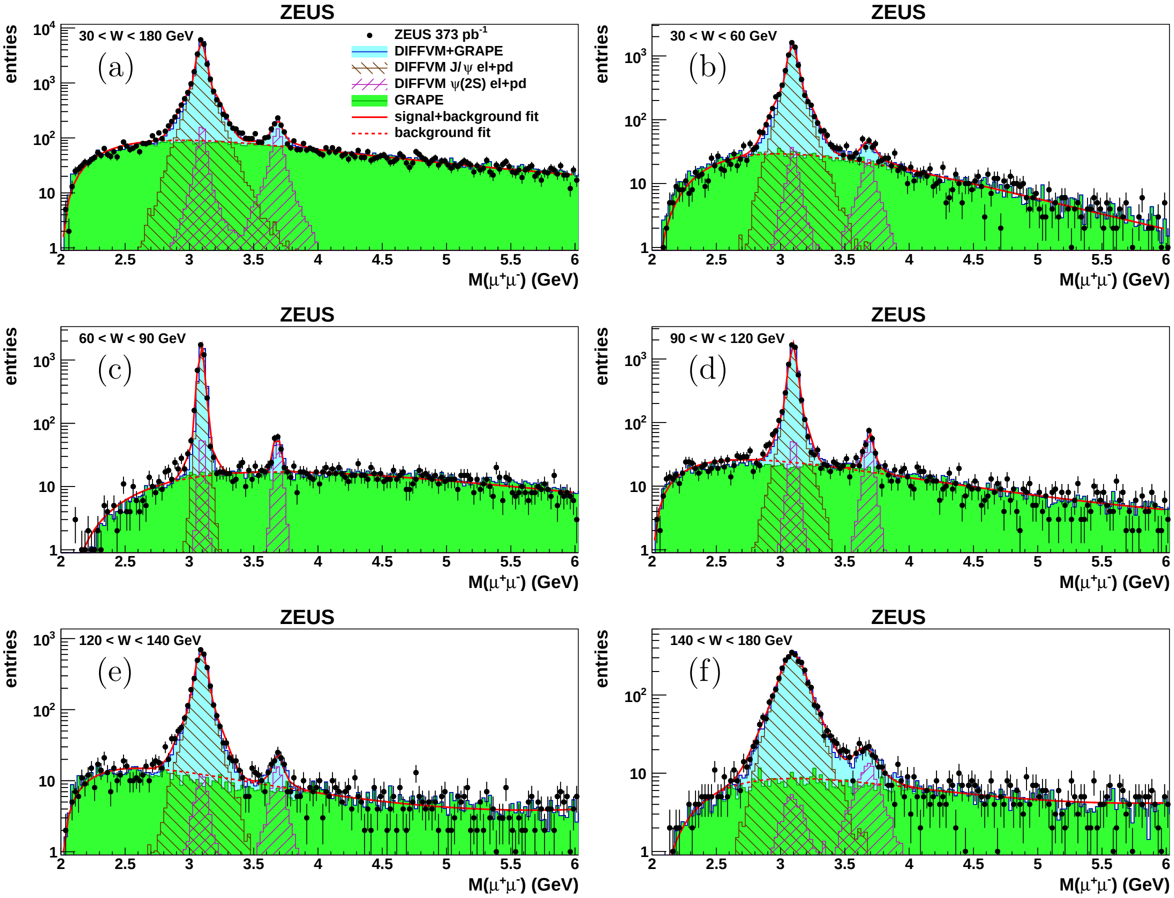

Figure 2: *Measured invariant mass distribution,* $M(\mu^+\mu^-)$*, of dimuon pairs (solid circles) in selected photoproduction events with error bars denoting statistical uncertainties. The data are shown in (a) the full* W *range,* $30 < W < 180$ *GeV, and (b) – (f) finer* W *intervals within the full range. Monte Carlo distributions for simulated events are shown for* DIFFVM *elastic and proton-dissociative processes of* $J/\psi(1S)$ *(brown hatched histogram) and* $\psi(2S)$ *(purple hatched histogram) and for a continuous background of muon pairs (*GRAPE*, green solid histogram) from the Bethe–Heitler process. The solid blue histogram represents the sum of all processes. The relative contribution of different processes was obtained from a fit to the data in the range* $2 < M(\mu^+\mu^-) < 6$ *GeV. The result of a double-Gaussian fit to the resonant peaks and parameterisation of the background, described in the text, is also shown (solid and dashed lines).*

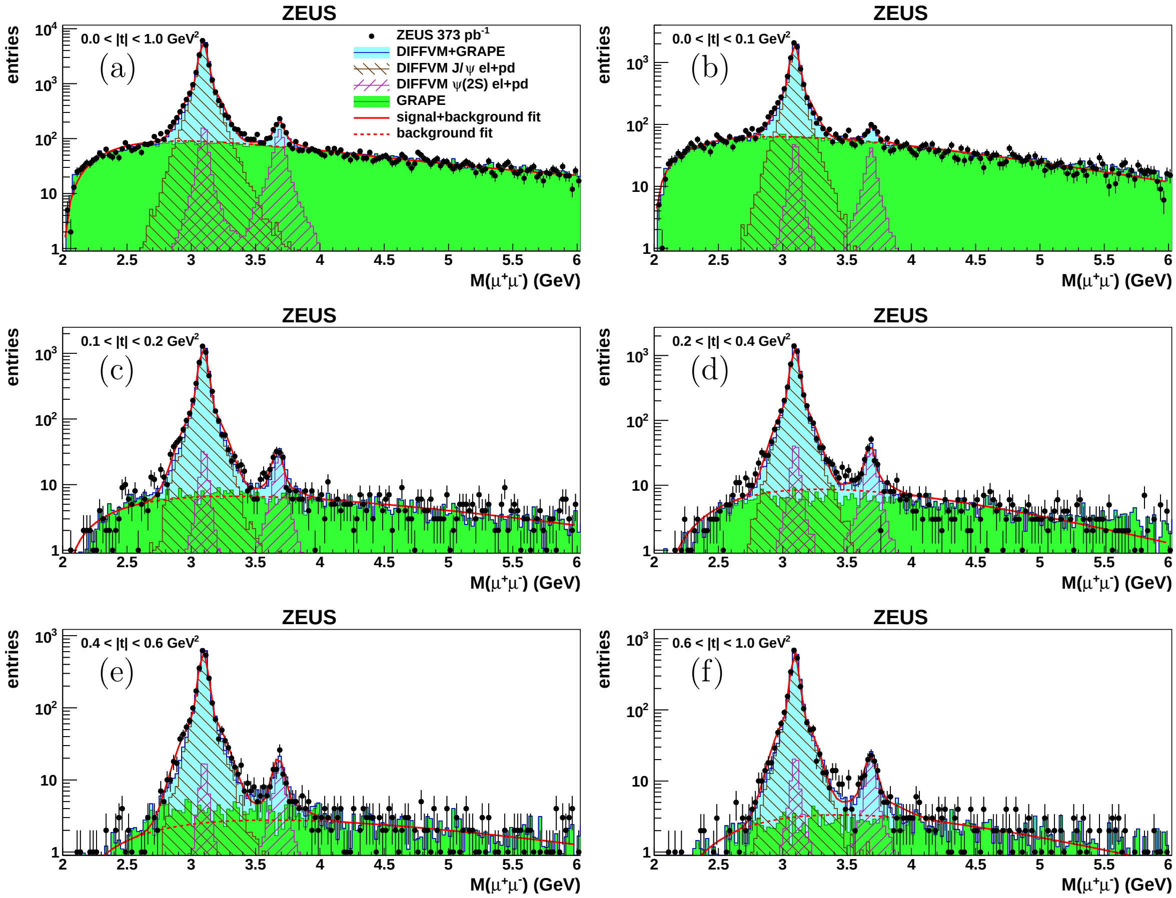

Figure 3: *Measured invariant mass distribution, $M(\mu^+\mu^-)$, of dimuon pairs (solid circles) in selected photoproduction events with error bars denoting statistical uncertainties. The data are shown in (a) the full $|t|$ range, $0.0 < |t| < 1.0\ GeV^2$, and (b) – (f) finer $|t|$ intervals within the full range. (Note that (a) shows the same data and simulations as Fig. 2(a) but is shown here again to highlight the $|t|$ dependence of the mass distributions.) All further details are as in the caption for Fig. 2.*

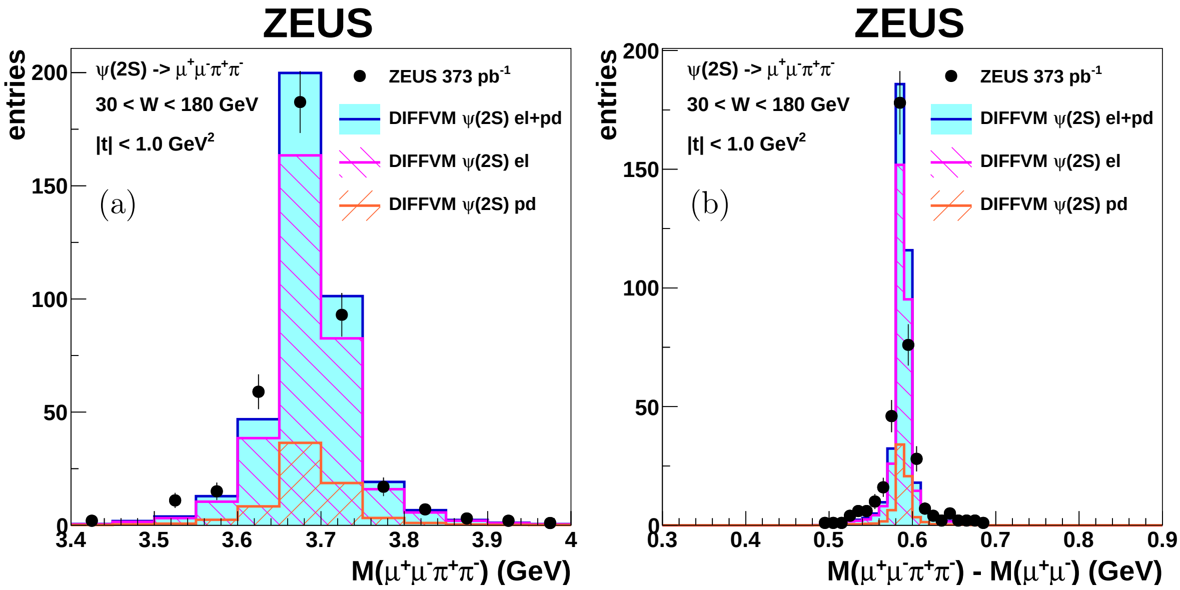

Figure 4: *(a) Measured invariant mass distribution, $M(\mu^+\mu^-\pi^+\pi^-)$, and (b) difference in invariant masses, $M(\mu^+\mu^-\pi^+\pi^-) - M(\mu^+\mu^-)$, for the 4-prong decay of $\psi(2S)$ in photoproduction events (solid circles), with error bars denoting statistical uncertainties. The invariant mass $M(\mu^+\mu^-)$ was required to be in the range $2.8 < M(\mu^+\mu^-) < 3.4$ GeV. Monte Carlo distributions for simulated events generated with* DIFFVM *are shown for elastic (magenta hatched histogram) and proton-dissociative (orange hatched histogram) processes of $\psi(2S)$ as well as their sum (blue solid histogram). The relative fraction of elastic and proton-dissociative processes was determined from a fit to the $|t|$ distribution.*

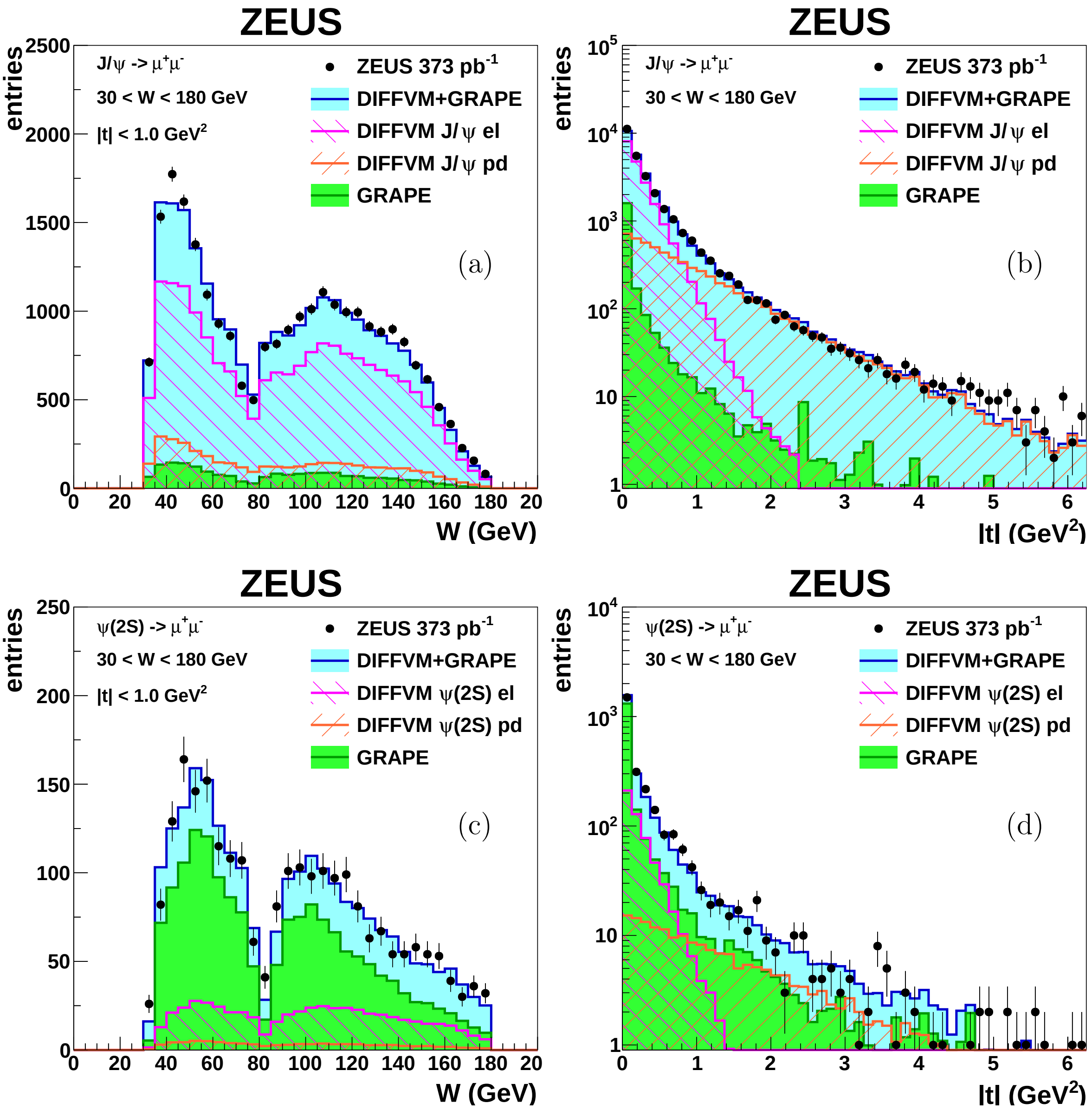

Figure 5: *Distributions of (a, c) W and (b, d) $|t|$ reconstructed for the decay of (a, b) $J/\psi(1S)$ and (c, d) $\psi(2S)$ mesons to a $\mu^+\mu^-$ pair in photoproduction events (solid circles), with error bars denoting statistical uncertainties.* DIFFVM *MC distributions for simulated events are shown for elastic (magenta hatched histogram) and proton-dissociative (orange hatched histogram) processes separately. The total sum of all contributions (blue solid histogram) as well as the* GRAPE *MC contribution from Bethe–Heitler processes (green solid histogram) is also shown.*

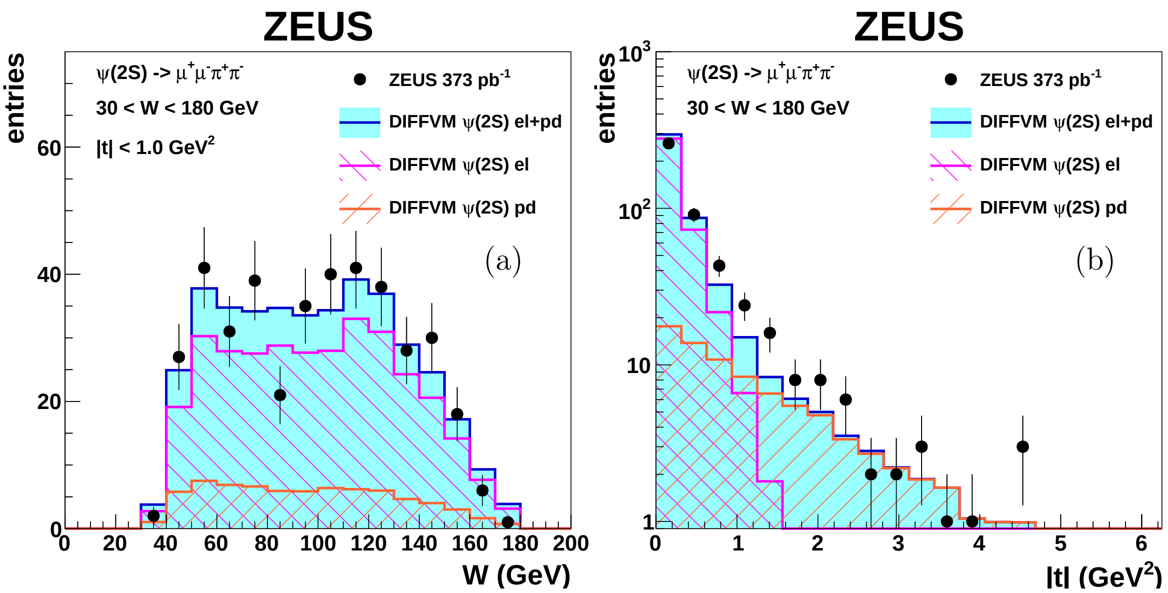

Figure 6: *Distributions of (a) W and (b) $|t|$ reconstructed for the 4-prong decay of $\psi(2S)$ in photoproduction events (solid circles), with error bars denoting statistical uncertainties. Details of the MC distributions for the 4-prong decay are as in the caption for Fig. 4.*

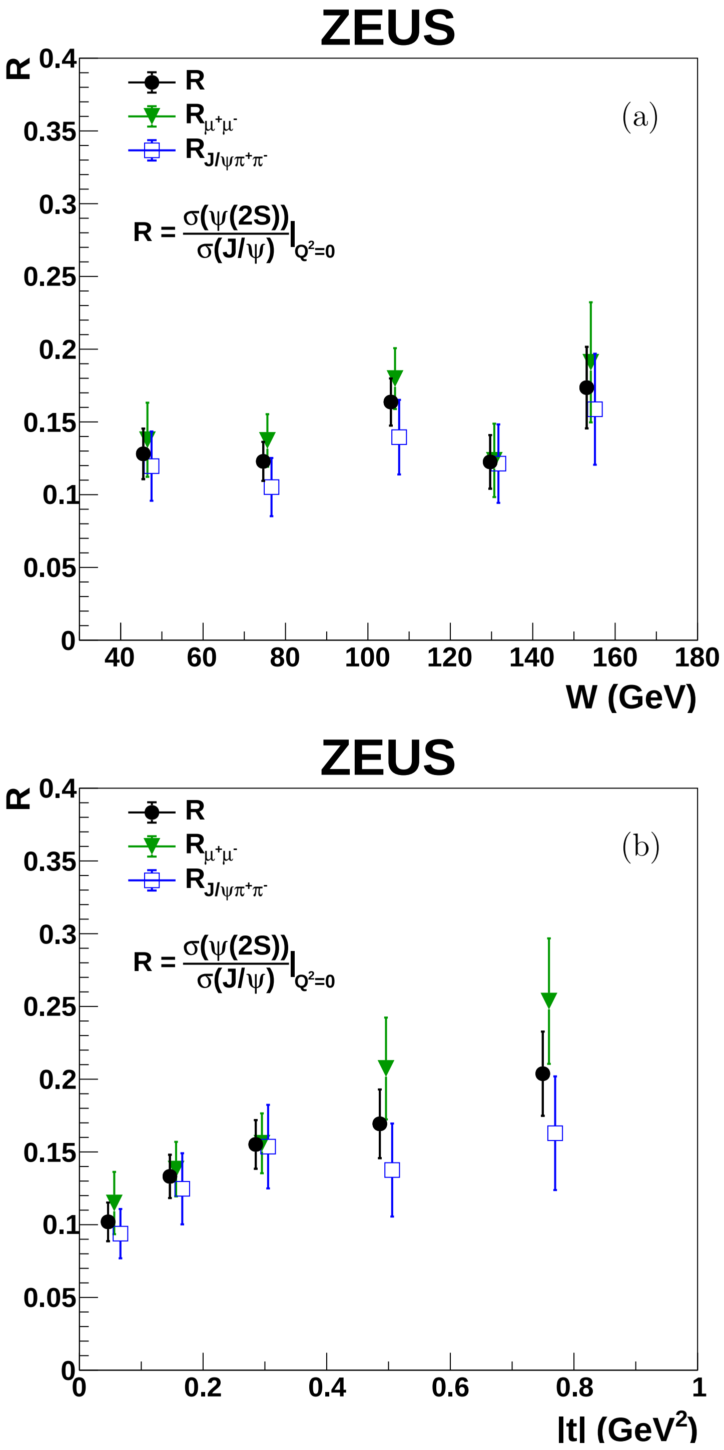

Figure 7: *Cross-section ratio* $R = \sigma_{\psi(2S)}/\sigma_{J/\psi(1S)}$ *in photoproduction as a function of (a)* W *and (b)* $|t|$ *for the two decay channels,* $R_{\mu\mu}$ *for* $\psi(2S) \to \mu^+\mu^-$ *(triangles) and* $R_{J/\psi\pi\pi}$ *for* $\psi(2S) \to J/\psi(1S)\,\pi^+\pi^-$ *(squares), and the combination of the two decay modes (solid circles). The error bars show the statistical uncertainties only. The points for* R *are shown at the mean* W *and* $|t|$ *values for each bin as determined for the* $J/\psi(1S)$ *data (see Table 1). The points for* $R_{\mu\mu}$ *and* $R_{J/\psi\pi\pi}$ *are displaced horizontally for better visibility.*

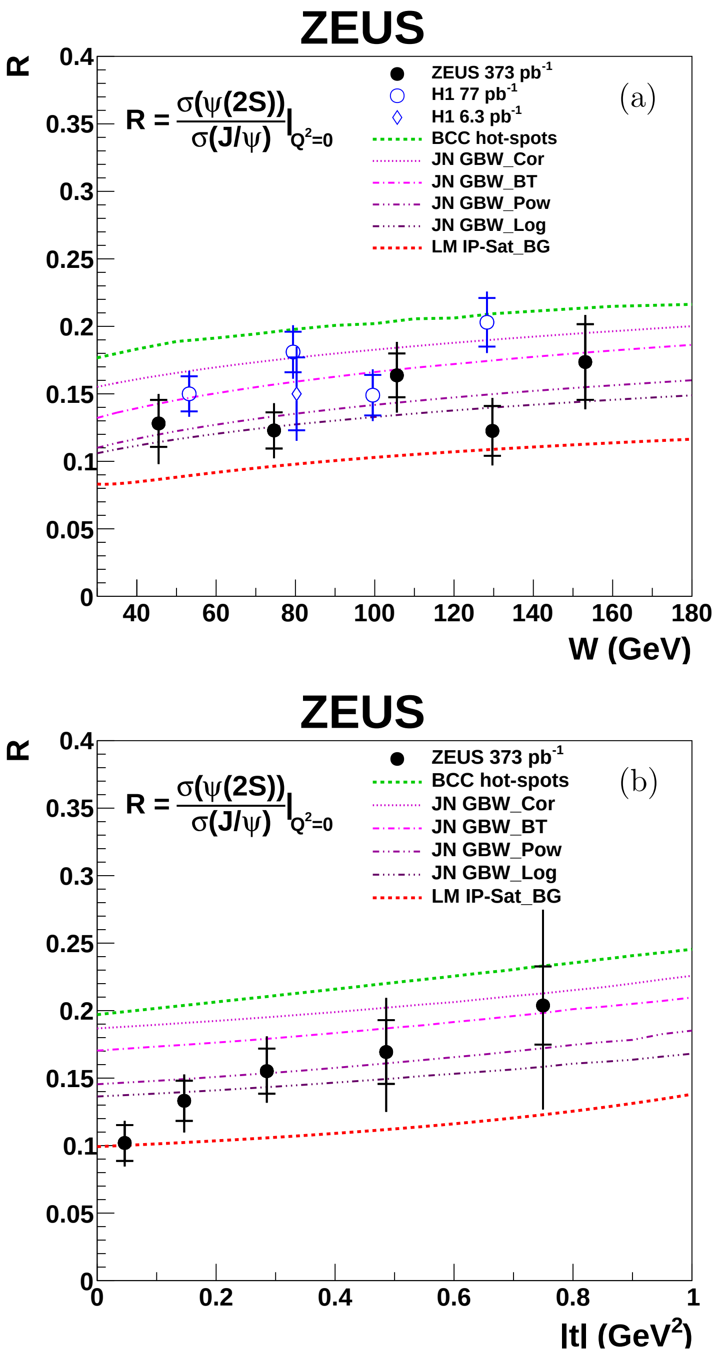

Figure 8: *Cross-section ratio* $R = \sigma_{\psi(2S)}/\sigma_{J/\psi(1S)}$ *in photoproduction for the combined* $\psi(2S)$ *decay modes as a function of (a)* W *and (b)* $|t|$*. The ZEUS measurements are shown as solid circles. The statistical uncertainties are shown as the inner error bars on the points whilst the outer error bars show the statistical and systematic uncertainties added in quadrature. The points are shown at the mean* W *and* $|t|$ *values for each bin as determined for the* $J/\psi(1S)$ *data (see Table 1). In (a) previous measurements from H1 (open points) [3, 4] are also shown. Various QCD-inspired models are compared to the data and shown as lines (see Section 7.1 for details of the models).*

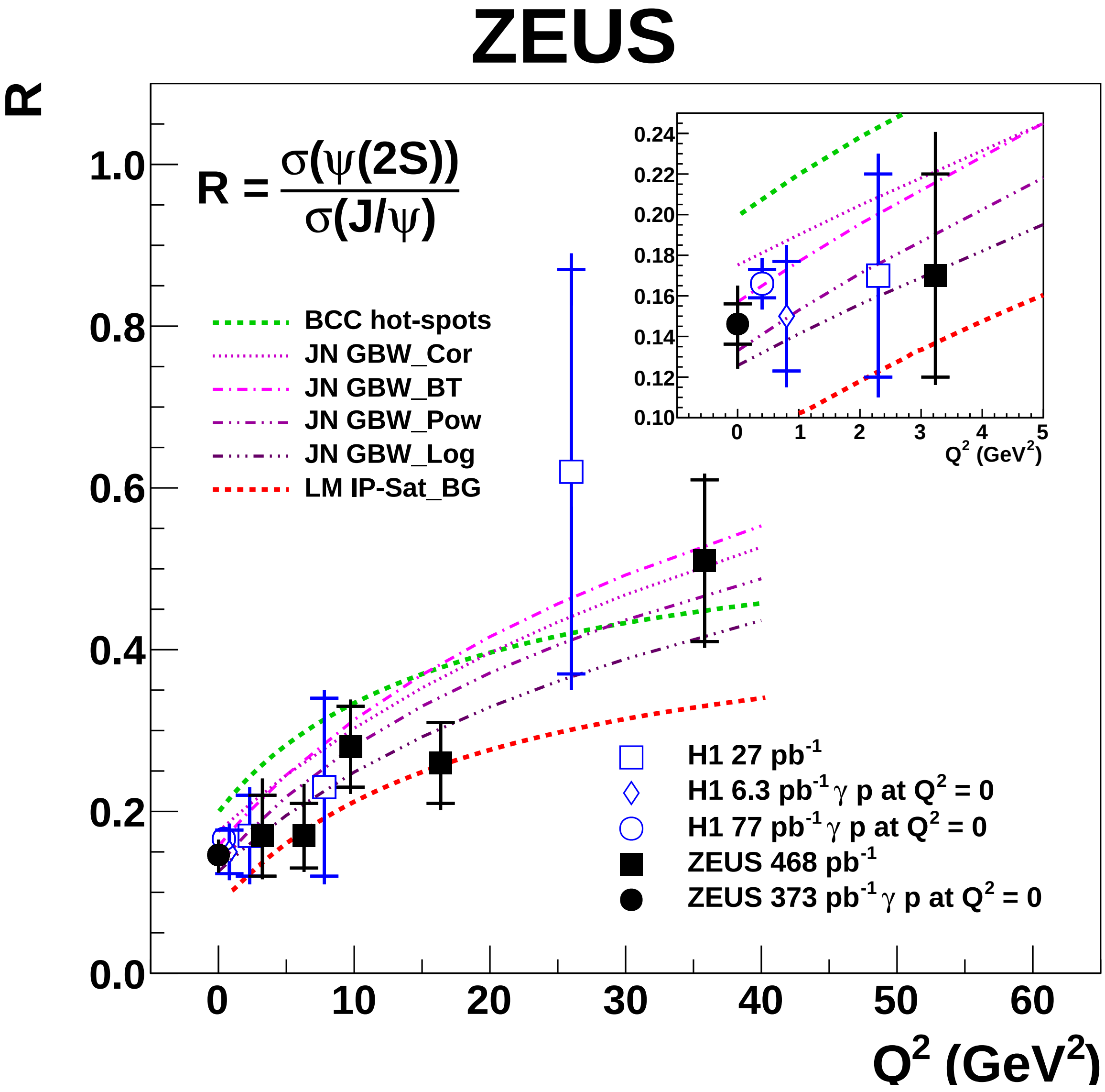

Figure 9: *Cross-section ratio* $R = \sigma_{\psi(2S)}/\sigma_{J/\psi(1S)}$ *as a function of* Q^2*. The measurement from this analysis of photoproduction data for the combined* $\psi(2S)$ *decay modes is shown at* $Q^2 = 0\ GeV^2$ *(solid circle). Previous measurements are also shown in photoproduction from H1 (open circle and diamond) [3, 4] which are plotted horizontally displaced for better visualisation and measurements from both H1 (open squares) [2] and ZEUS (solid squares) [1] in deep inelastic scattering. The inset shows a zoom-in of the region at low* Q^2 *for better visibility. The statistical uncertainties are shown as the inner error bars on the points whilst the outer error bars show the statistical and systematic uncertainties added in quadrature. Various QCD-inspired models are compared to the data and shown as lines (see Section 7.1 for details of the models).*